SUPPLEMENTARY MATERIAL

Metallic Behavior in STO/LAO Heterostructures with Non-Uniformly Atomic Interfaces

Rafael A.C. Amoresi[1,2*], Leonélio Cichetto Jr.[2,3], Amanda F. Gouveia[4], Yormary N. Colmenares[5], Marcio D. Teodoro[3], Gilmar E. Marques[3], Alexandre Z. Simões[1], Juan Andres[2], Elson Longo[4], Adenilson J. Chiquito[3], Maria A. Zaghete[6]

[1]*Faculty of Engineering of Guaratinguetá, São Paulo State University – UNESP, 12516-410, Guaratinguetá, SP, Brazil*

[2]*Department of Analytical and Physical Chemistry, University Jaume I (UJI), Castello 12071, Spain*

[3]*Department of Physics Federal University of São Carlos - UFSCAR, 13565-905 São Carlos, SP, Brazil*

[4]*CDMF, Federal University of São Carlos - UFSCAR, 13565-905 São Carlos, SP, Brazil*

[5]*Institute of Physics of São Carlos, University of São Paulo - USP, 13560-970, São Carlos, Brazil*

[6]*Interdisciplinary Laboratory of Electrochemistry and Ceramics, LIEC – Chemistry Institute, São Paulo State University – UNESP,14800-060, Araraquara, SP, Brazil*

**rciola@uji.es; rafaelciola@yahoo.com.br*

AFM and XRD

Figure S1 shows the surface topography obtained by AFM for the two sets of films used. The AFM investigation of the films revealed the formation of small grains sized ~25 nm with a typical roughness (R_{ms}) of ~0.584 nm for the non-oxygenated system, as seen in Figure S1b; a mean grain size of around 50 nm and R_{ms}~0.543 nm were obtained for the oxygenated system (Figure S1c). In the non-oxygenated film, it is possible to clearly distinguish the grain boundaries, whereas in the oxygenated film, the grain boundary is much less defined. Both films have a roughness between 0.4 and 1.2 nm, which implies that they are smooth films presenting very small grains, indicating a pseudo 2D growth mode (Stranski–Krastanov)[1]. As verified in previous studies[1–3], low roughness films (quadratic roughness less than 1.0 nm) imply atomically smooth surfaces with layer-by-layer growth modes. These factors are mainly observed in the oxygenated film that shows less roughness and an absence of defined grain boundaries. Consequently, it is in this film on which the 2DEG is observed.

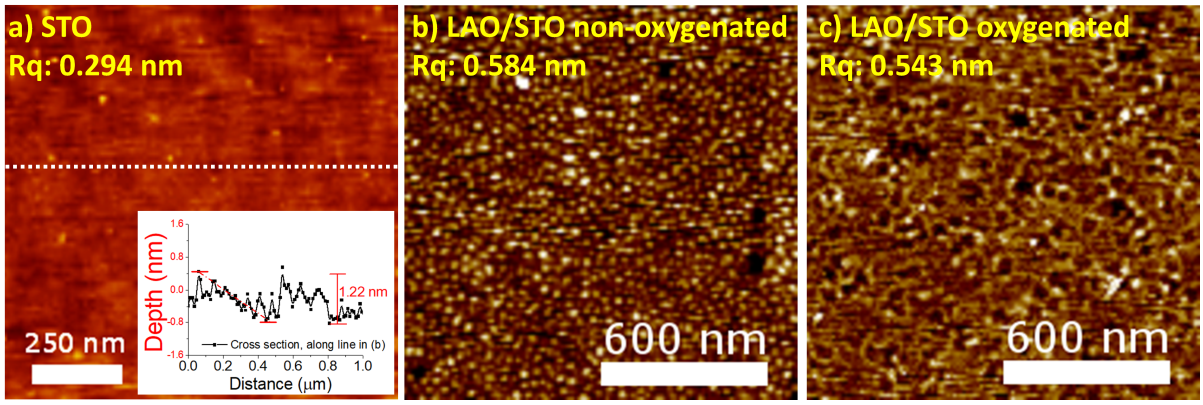

Figure S1. 2D AFM image for the a) STO substrate, b) oxygenated and c) non-oxigenated LAO/STO heterostrucuture.

Raman spectroscopy was performed to investigate the short-range structural order of metallic and insulator sample, Figure S2a. This analysis show in a different way than previously reported in the literature, the relationship between the electrical behavior of the different modes

of growth of the heterostructure and the interaction between the LAO and STO materials. STO at room temperature has an ideal cubic perovskite structure, where there are five atoms per unit cell, each one located at a point of the inverse symmetry. Therefore, in the center of the Brillouin zone, all the optical phonon modes in the cubic phase have odd parities and first-order Raman scatterings (TO_m, LO_n) are forbidden.[4] In this way, the spectrum will be dominated by second-order scatterings. The optical phonons appear at 87 (TO1), 179 (LO1, TO2), 472 (LO2), 542 (TO3), 792 (LO3) cm^{-1}, and 265 cm^{-1} for the F_{2g} mode,[5] where the TO and LO modes are transverse optical and longitudinal optical modes, respectively.

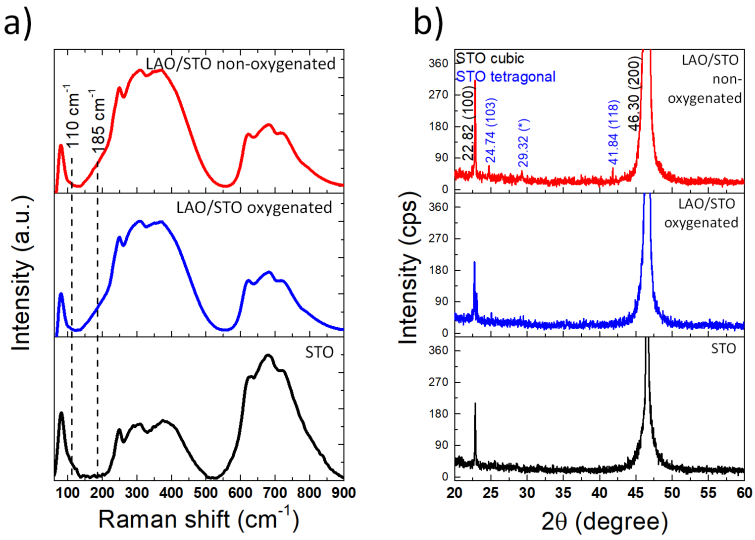

Figure S2. Structural analysis of the substrate and both sets of samples, a) Raman scattering spectra characterizing the vibrational modes of the samples. The dotted lines illustrate the difference between the substrate and the heterostructures, and b) X-ray patterns of the samples.

In our case, a scattering Raman located in range 70–120 $cm^{-1}$is observed for the single crystal. It is correlated to the TO1 mode, and the broadening of the modes in the 235–445 cm^{-1} and 625–725 cm^{-1} ranges are related to the longitudinal optical modes. The transverse optical modes at 179 cm^{-1} and 545 cm^{-1} are forbidden by symmetry for single crystals;[6] thus, they do

not appear in our results. It is observed that in the heterostructure there is formation of a mode at 185 cm^{-1} and the suppression of the mode at 110 cm^{-1} compared to the STO monocrystal. The LAO shows the A_{1g} modes occurring at 125 cm^{-1} that can be associated with the rotation of the octahedral oxygen around the hexagonal direction $[001]_h$; two E_g modes around 155 cm^{-1} relative to pure La vibrations in the hexagonal plane $(001)_h$; and another one at 488 cm^{-1} related to vibrations of oxygen flexion.[7,8] It is clear in our results that the E_g mode at 185 cm^{-1}, indicative of vibrations of La, is observed in the spectrum of the heterostructures. The E_g modes are related to doubly degenerate states caused by polarizabilities, α_{xx} and α_{xy}, which in turn suggests that the heterostructured film should present a vibrational degree of freedom with respect to the axis of symmetry in the *xy* plane. However, the A_{1g} mode of LAO in the 110 cm^{-1} region is suppressed in the heterostructured film. This phenomenon may occur because this mode exhibits a symmetry displacement character along the *c*-axis of the LAO structure that is possibly in resonance with the STO transverse optical mode. As a consequence, vibrations of the oxygen atoms in the LAO axis of symmetry and those from the STO adjacent atoms cancel the vibrational degree of freedom.[9–11] Comparing the 200–500 cm^{-1} and 600–800 cm^{-1} modes of the heterostructure with those of STO, a change in their intensity can be observed. Vibrational modes related to bending (~450 cm^{-1}) and stretching (~740 cm^{-1}) for octahedral $[BO_6]$ clusters are usually assigned to these regions[8,12]. Therefore, the stretching vibrational modes decrease considerably with respect to the bending modes, indicating that the formation of the heterostructure takes place along the *c*-axis. Furthermore, the vibrational modes at 180 cm^{-1}, the suppressed ones at 110 cm^{-1}, and the difference in the intensity of the 450/740 cm^{-1} modes when comparing heterostructures and substrates are evidence that support the idea of interface interactions between adjacent clusters on the *c*-axis during the heterojunction formation.

Figure S2b shows the long-range analysis through the diffractograms for the STO substrate and the oxygenated and non-oxygenated systems. Peaks related to the substrate diffractogram

coincide with those of the cubic monocrystalline (001) structure from the ICSD database CIF n° 23076 for STO. For both systems (oxygenated and non-oxygenated), peaks related to the cubic phase of the STO are also observed; however, to non-oxygenated sample the presence the others peaks suggest the presence of secondary phases probably related to the different metals interdiffusion at the interface.

PL

The PL emission spectra were deconvoluted to further elucidate the emission centers and to qualitatively determine the contribution of each visible light component at two temperatures, 10 K and 150 K. **Figure S2** illustrates the results obtained from these deconvolutions, and the profiles are described well by the Voigt area function.

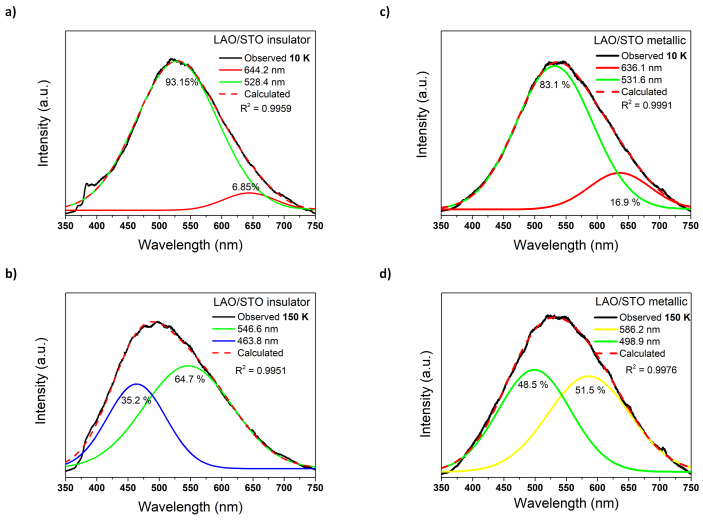

Figure S3. Deconvolution of the PL spectra to the 10 K and 150 K temperatures of the insulator and metallic systems. The spectra show the different emission regions with the main highlight for the insulator sample that suggests emission in the region of the vacancies of the monoionized type (blue region).

Computational procedure and model systems

Theoretical models were constructed to analyze how the formation of the 2DEG occurs at the atomic level and to rationalize the experimental results. The three-dimensional connectivity of both dodecahedra [AO_{12}] and octahedral [BO_6] clusters in ABO_3 perovskites can result in a range of properties, including conductor-like and magnetic behaviors. By this mechanism, combinations of structural and electronic distortions (e.g. octahedral tilts, O−A−O and O−B−O bending movements, etc.) can break the inversion symmetry to render polar structures. These distortions can be considered as symmetry breaking distortion modes applied to the parent high symmetry structure, whose amplitude indicates the magnitude of the distortion from the high symmetry model. These modes are responsible for the appearance of new electronic properties, which are a result of the distortions.

Therefore, first-principle calculations for the LAO/STO heterostructure were performed using DFT as implemented in the Vienna *Ab-initio* simulation package (VASP) program.[13,14] The Kohn–Sham equations were solved using the Perdew–Burke–Ernzerhof (PBE) functional,[15] and the electron-ion interactions were described using the projector-augmented wave pseudopotentials.[13,16] The plane-wave expansion was truncated at a cutoff energy of 520 eV, and the Brillouin zones were sampled through 4 × 4 × 1 Monkhorst–Pack special k-point grids that ensured geometrical and energetic convergence for the LAO/STO heterostructure.

First of all, the lattice parameters and internal coordinates of the LAO and STO bulk were optimized. Both perovskites belong to the same spacial group and have a similar lattice parameter. Hence, to construct the LAO/STO heterostructure in the (100) direction, a convergence energy test for the lattice parameter was performed, comparing the final energy of the optimized bulk parameter. Thus, the lattice parameter (a) used for the LAO/STO heterostructure models was a = 3.8276 Å. The experimental results revealed that the STO surface was thicker than the LAO surface. Therefore, to construct the models, a five-layer

model for LAO and an eleven-layer model for STO were used. Several models that combine the two interfaces of each systems were constructed to study the LAO/STO heterostructure: $(LaO)^{+}-(SrO)^{0}$, $(LaO)^{+}-(TiO_2)^{0}$, $(AlO_2)^{-}-(TiO_2)^{0}$,and $(AlO_2)^{-}-(SrO)^{0}$ surface termination. A vacuum spacing of 15 Å was introduced in the z-direction in order to prevent an interaction from occurring between both surfaces.

The theoretical calculations were also used to study the effect of symmetry and stoichiometry on the formation of the LAO/STO heterostructures. The two surface models were separated by distance of 2.000 Å before optimization (unrelaxed structure), which is a close value for bonds found in materials. In the optimization process, the entire LAO/STO heterostructure was allowed to relax.

The theoretical LAO/STO heterostructure calculations stared with the model illustrated on Figure S3. The LAO film contained five atomic layers alternating between $(LaO)^{+}$ and $(AlO_2)^{-}$, while the STO substrate contained eleven layers alternating between $(SrO)^{0}$ and $(TiO_2)^{0}$, were used for of the LAO/STO interface, which are models symmetric and non-stoichiometric.

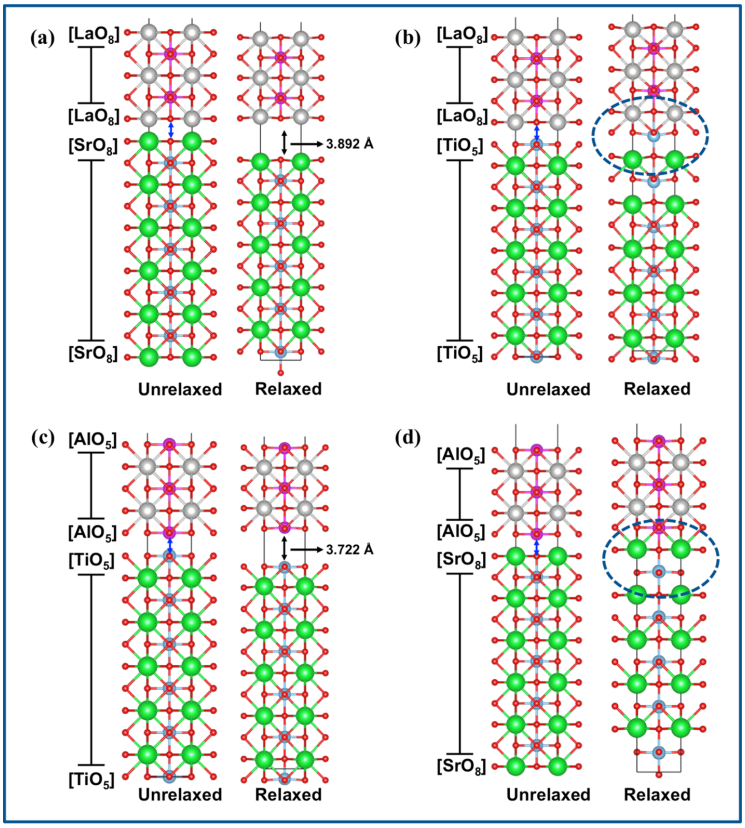

Figure S4. Theoretical models oftheLAO/STO heterostructure with different kinds of interface interactions: **(a)** $[SrO_8] - [LaO_8]$, **(b)**$[TiO_5] - [LaO_8]$, **(c)**$[TiO_5] - [AlO_5]$, and **(d)**$[SrO_8] - [AlO_5]$. The green, blue, lilac, gray, and red represent the Sr, Ti, Al, La and O atoms, respectively.

In the next step, the values of the Mulliken charge of each interface were observed to increase with the interatomic distance, as illustrated in Figures S4.

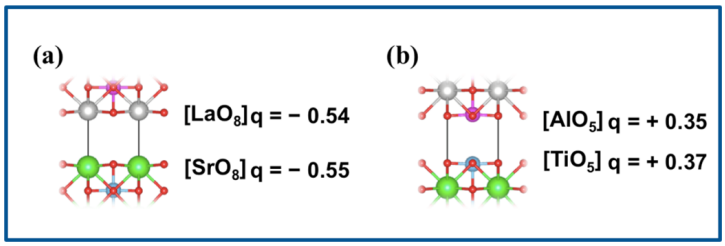

Figure S5. Calculated Mulliken charge for the clusters on the interface in the models of the LAO/STO heterostructure: **(a)** $[SrO_8] - [LaO_8,]$ and**(b)** $[TiO_5] - [AlO_5]$. The green, blue, lilac, gray, and red represent the Sr, Ti, Al, La and O atoms, respectively.

From these theoretical results, three more models were constructed to analyze the effect of excess O anions on the upper part of the heterostructure, simulating the experimental condition for the oxygenated system of the LAO/STO heterostructure, and the effect of the stoichiometry on the results (Figure S6).

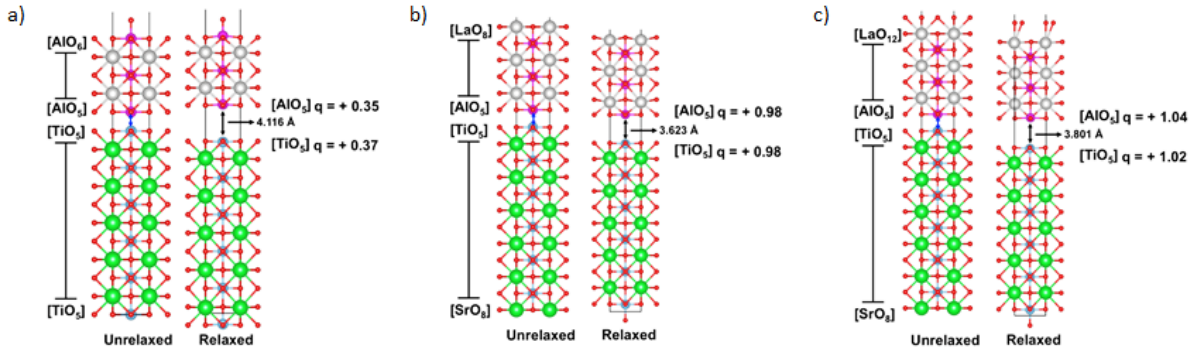

Figure S6. Theoretical models of the LAO/STO heterostructure with excess of O atoms and the stoichiometry system: **(a)** $[AlO_5] - [TiO_5]$ oxygenated, **(b)** Stoichiometry system non-oxygenated, and **(c)** Stoichiometry system oxygenated. The green, blue, lilac, gray, and red represent the Sr, Ti, Al, La and O atoms, respectively.

References

1 M. Golalikhani, Q. Y. Lei, M. A. Wolak, B. A. Davidson and X. X. Xi, *J. Cryst. Growth*, 2016, **443**, 50–53.

2 M. Golalikhani, Q. Y. Lei, G. Chen, J. E. Spanier, H. Ghassemi, C. L. Johnson, M. L. Taheri and X. X. Xi, *J. Appl. Phys.*, 2013, **114**, 27008.

3 F. C. Frank and J. H. van der Merwe, *Proc. R. Soc. A Math. Phys. Eng. Sci.*, 1949, **198**, 205–216.

4 Y. Zhang, S. L. Li, J. Li, H. Deng, L. M. Cui and D. N. Zheng, *Appl. Phys. Lett.*, 2012, **101**, 43502.

5 V. N. Denisov, B. N. Mavrin and V. B. Podobedov, *Phys. Rep.*, 1987, **151**, 1–92.

6 V. I. Merkulov, J. R. Fox, H.-C. Li, W. Si, a. a. Sirenko and X. X. Xi, *Appl. Phys. Lett.*, 1998, **72**, 3291–3293.
7 V. G. Sathe and A. Dubey, *J. Phys. Condens. Matter*, 2007, **19**, 382201.
8 M. V. Abrashev, A. P. Litvinchuk, M. N. Iliev, R. L. Meng, V. N. Popov, V. G. Ivanov, R. A. Chakalov and C. Thomsen, *Phys. Rev. B*, 1999, **59**, 4146–4153.
9 M. Grzeszczyk, K. Gołasa, M. Zinkiewicz, K. Nogajewski, M. R. Molas, M. Potemski, A. Wysmołek and A. Babiński, *2D Mater.*, 2016, **3**, 25010.
10 E. Altendorf, X. K. Chen, J. C. Irwin, R. Liang and W. N. Hardy, *Phys. Rev. B*, 1993, **47**, 8140–8150.
11 X. Zhang, X.-F. Qiao, W. Shi, J.-B. Wu, D.-S. Jiang and P.-H. Tan, *Chem. Soc. Rev.*, 2015, **44**, 2757–2785.
12 C. Aruta, M. Angeloni, G. Balestrino, N. G. Boggio, P. G. Medaglia, A. Tebano, B. Davidson, M. Baldini, D. Di Castro, P. Postorino, P. Dore, A. Sidorenko, G. Allodi and R. De Renzi, *J. Appl. Phys.*, 2006, **100**, 23910.
13 G. Kresse and J. Furthmiiller, *Comput. Mater. Sci.*, 1996, **6**, 15–50.
14 G. Kresse and J. Hafner, *Phys. Rev. B*, 1994, **49**, 14251–14269.
15 J. P. Perdew, K. Burke and M. Ernzerhof, *Phys. Rev. Lett.*, 1996, **77**, 3865–3868.
16 G. Kresse and D. Joubert, *Phys. Rev. B*, 1999, **59**, 1758–1775.